DEVELOPMENTAL BIOLOGY

A fibronectin gradient remodels mixed-phase mesoderm

Min Zhu[1], Bin Gu[2], Evan C. Thomas[1], Yunyun Huang[1,3], Yun-Kyo Kim[1], Hirotaka Tao[1], Theodora M. Yung[1], Xin Chen[1], Kaiwen Zhang[1,4], Elizabeth K. Woolaver[1,5], Mikaela R. Nevin[1,5], Xi Huang[1,5], Rudolph Winklbauer[4], Janet Rossant[1,5], Yu Sun[3]*, Sevan Hopyan[1,5,6]*

Copyright © 2024 The Authors, some rights reserved; exclusive licensee American Association for the Advancement of Science. No claim to original U.S. Government Works. Distributed under a Creative Commons Attribution NonCommercial License 4.0 (CC BY-NC).

Physical processes ultimately shape tissue during development. Two emerging proposals are that cells migrate toward stiffer tissue (durotaxis) and that the extent of cell rearrangements reflects tissue phase, but it is unclear whether and how these concepts are related. Here, we identify fibronectin-dependent tissue stiffness as a control variable that underlies and unifies these phenomena in vivo. In murine limb bud mesoderm, cells are either caged, move directionally, or intercalate as a function of their location along a stiffness gradient. A modified Landau phase equation that incorporates tissue stiffness accurately predicts cell diffusivity upon loss or gain of fibronectin. Fibronectin is regulated by WNT5A-YAP feedback that controls cell movements, tissue shape, and skeletal pattern. The results identify a key determinant of phase transition and show how fibronectin-dependent directional cell movement emerges in a mixed-phase environment in vivo.

INTRODUCTION

Although cell division underlies growth, morphogenesis involves fundamentally physical processes that form the embryo. Cell movements, rather than the spatial distributions of cell divisions, are often responsible for shaping various embryonic structures (*1*, *2*). Long-range coordination of morphogenetic cell movements shapes the main body axis (*3*), the face (*2*), limbs (*4*), skin (*5*), and other organ primordia (*6*). Biochemical cues such as morphogens, chemoattractants, and cell polarity pathways (*6*, *7*) do not fully explain long-range cell coordination in vivo, in part, because of the short range (*8*) and noisy nature (*9*) of diffusible ligand gradients. During early outgrowth of murine limb bud that is composed of a volume of mesoderm that arises from the lateral plate and is covered by a single-cell layer of ectoderm, at least some well-characterized secreted ligands do not attract mesodermal cells (*10*) and the three-dimensional (3D) cell movement pattern does not correspond to the spatial domains of candidate chemoattractants such as *Wnt5a* (*4*). Physical cues such as tissue stiffness represent alternative candidate mechanisms that can be communicated rapidly among many cells over long distances (*4*, *11*). Likely, a combination of mechanisms fully explains morphogenesis (*12*).

Phase transition is a relatively recent and potentially useful framework to describe cell and tissue movements (*13*, *14*). The concept is based, in part, on the physics of foams to explain the frequency of cell rearrangements and has been assessed as a function of cellular parameters (*3*, *13*, *15*, *16*). This paradigm has been applied to describe elongation of the zebrafish tail bud (*3*), vertebrate digit primordia (*17*), and the mandibular arch of the mouse embryo (*4*). In the theoretical case of confluent cells, tissue phase can be determined by cell geometries (*15*) although most tissues are not truly confluent. Jamming is another type of phase transition in which cell packing corresponds to tissue formation although mechanistic explanations for this phenomenon are incomplete. Jamming correlates with the degree of cell-cell proximity (connectivity) (*13*) or adhesion (*3*) in zebrafish. In contrast to particulate (multicellular) (*13*) or continuum (bulk tissue) (*3*) models that have been used to describe phase transition, tissues typically contain both cells and substrates that profoundly impact material properties. The contribution of substrates to tissue phase has not been described. Moreover, although tissue stiffness corresponds to cell jamming (*3*), the relationship between material tissue properties and tissue phase remains incompletely understood.

Durotaxis is a distinct hypothesis that has been used to explain the directional movement of cells. As has been shown primarily in vitro (*18*), cells often preferentially move toward stiffer substrate. Evidence for durotaxis in vivo was shown during neural crest cell migration in *Xenopus* (*12*, *19*) and in correlative findings in our previous work on the mouse limb bud showing that mesodermal cells move up a tissue stiffness gradient (*4*). However, experiments that supported durotaxis in *Xenopus* involved epithelial dissection and used surface indentation to measure subsurface stiffness gradients, thereby introducing variables such as tissue integrity and measurement resolution in deep tissue (*12*, *19*). Nonetheless, durotaxis is an important consideration, especially in a mixed-phase environment in which a stiffness gradient would be expected to interpolate between liquid-like and solid-like states, a possibility that has not been explored.

Here, we used live light sheet imaging of mouse embryos harboring transgenic markers and endogenous protein reporters to demonstrate the relationship between cell movements and FN-dependent stiffness. Cells in the stiffest and softest regions of limb bud mesoderm exhibited caged or rearranging behaviors, respectively, with low directional persistence (a measure of directional constancy). In the intervening region where a stiffness gradient dominates, cells moved in a coordinated, durotaxis-like manner with high persistence.

[1]Program in Developmental and Stem Cell Biology, Research Institute, The Hospital for Sick Children, Toronto, ON M5G 0A4, Canada. [2]Department of Obstetrics Gynecology and Reproductive Biology, and Institute for Quantitative Health Science and Engineering, Michigan State University, East Lansing, MI 48824, USA. [3]Department of Cell and Systems Biology, University of Toronto, Toronto, ON M5S 3G5, Canada. [4]Department of Mechanical and Industrial Engineering, University of Toronto, Toronto, ON M5S 3G8, Canada. [5]Department of Molecular Genetics, University of Toronto, Toronto, ON M5S 1A8, Canada. [6]Division of Orthopaedic Surgery, The Hospital for Sick Children and University of Toronto, Toronto, ON M5G 1X8, Canada.
*Corresponding author. Email: sevan.hopyan@sickkids.ca (S.H.); yu.sun@utoronto.ca (Y.S.)

We tested for a causal relationship between tissue stiffness and cell movements by performing conditional loss and gain of function experiments using a floxed fibronectin (*Fn*) and a new knock-in Fn overexpression strain that we generated. A modification of the Landau theory for second-order phase transitions with a term describing the coupling of cellular diffusion to a stiffness gradient accurately predicted cell diffusivity upon loss and gain of fibronectin. Using additional mutants, we found that FN is downstream of a WNT5A-YAP pathway and feeds back to promote yes-associated protein 1 (YAP) nuclear translocation and *Wnt5a* expression. The results identify extracellular matrix (ECM) abundance as a determinant of phase transition and show how directional cell movement emerges in a mixed-phase environment to shape tissue shape in vivo.

RESULTS

Modes of mesodermal cell movements vary as a function of tissue stiffness

To obtain a 3D tissue stiffness map, we used a 3D magnetic tweezer system that we developed previously (*4*). By generating a uniform magnetic field gradient within the workspace, magnetic beads injected in the E9.25 (embryonic day 9.25) mouse limb bud were actuated with identical forces (Fig. 1A). Local tissue stiffness was quantified by fitting the bead displacement-time curve using a Zener model with a serial dashpot. To merge tissue stiffness maps obtained from different embryos while avoiding data skewing by sub-somite stage differences in limb bud morphologies, we devised a method of registering 3D limb bud shape using a customized program (Materials and Methods; fig. S1, A to C; and movie S1) (*20*). As before (*4*), we confirmed that the 21 somite (som., ~E9.25) mouse limb bud exhibited an anteroproximally biased mesodermal stiffness gradient (Fig. 1B and fig. S1D).

We examined the relation between tissue stiffness and cell movements by performing live, time-lapse light sheet microscopy (*2*, *4*) of embryos harboring a transgenic far-red nuclear reporter H2B-miRFP703 (*21*). The resulting movies revealed previously unattainable detail due to our ability to identify and track nearly every nucleus deep within mesoderm. After correcting for embryo drift by tracking fluorescent beads implanted in the agarose cylinder immediately surrounding the embryo, we observed that large-scale cell movements flowed toward and around the stiff core (Materials and Methods, Fig. 1C, and movie S2).

To understand how the curious vortex-like pattern of cell movement contributes to limb bud outgrowth, we computed the angular momentum of each cell with respect to a coordinate origin that we defined as the point at which cells moved the least (less than 3% of maximum motion, in the center of the vortex). The average angular momentum was directed distally, helping to explain the longitudinal axis of growth. To better understand how mesodermal cell movements shape the limb bud, we expanded every cell's vector according to cylindrical coordinates using the average angular momentum as a reference axis. By separately plotting the longitudinal (i.e., parallel to the longitudinal cylindrical axis) and radial (i.e., perpendicular to the cylindrical axis) vector components for every cell, we identified motions that were previously obscured by the overall swirling pattern. Along the longitudinal cylindrical axis, proximodistal mesodermal cell movements tended to elongate the limb bud. Along the radial axis, cells in the proximal and distal aspects of the bud moved toward and away from the center of the bud, respectively (fig. S1E). Together, these motions suggest an overall pattern of 3D convergent extension that is consistent with the recognized anisotropic growth of the limb bud (fig. S1F).

To understand the basis of the cell movement pattern, we examined various parameters. The spatial distributions of the mesodermal cell-cell adhesion protein N-cadherin, motor protein phospho-myosin light chain, cell packing density (*4*), and intercellular space quantified using transmission electron microscopy (TEM) were spatially uniform within mesoderm. Mean cortical tension as estimated by a transgenic vinculin tension sensor (*2*) exhibited only a mild peripheral gradient near the ectoderm and no anteroposterior gradient (fig. S2). These findings do not rule out regulation of the coordinated cell movement pattern that we observed by mechanisms such as cell sorting or spatially biased cell adhesion. We chose to focus on the potential role of mesodermal stiffness because that gradient qualitatively corresponds best with the pattern of cell movements that we observed.

To quantify mesodermal cell displacements, we first calculated cell migration persistence. Persistence is defined as the magnitude of the overall (start-to-finish) cell displacement vector divided by the total length of the displacement trajectory ranging from 0 (random motion) to 1 (straight-line motion) (Fig. 1D and fig. S3A) (*22*). By registering the tissue stiffness map to the persistence map to examine spatial correlation between the two parameters, we identified a continuum of cell movement types that we categorized into three distinct zones (fig. S3B). In the stiff core (zone 1) where effective stiffness was greater than 1.5×10^{-3} as well as in the soft region furthest from the stiff core (zone 3), cells exhibited low migration persistence. In contrast, cells immediately surrounding the stiff core where a stiffness gradient was present (zone 2) migrated with high persistence (Fig. 1E and movie S3). By performing 3D limb bud shape registration, we quantitatively compared the persistence maps measured from different embryos and found the mean SD to be around 10%, indicating that the spatial pattern of cell migration persistence was fairly consistent across different embryos (Materials and Methods and fig. S3, C to E). We also plotted mean square displacement (MSD) that represents the deviation of position with respect to a reference position over time as a measure of the spatial extent of random cell motion. A slope of 1 represents the diffusion of water, whereas higher and lower slopes reflect ballistic and relatively static behaviors, respectively. We identified three regionally distinct slopes of strong subdiffusion, superdiffusion, and relatively weak subdiffusion that corresponded to stiff, gradient, and soft regions of mesoderm (fig. S3F). Together, these analyses suggested that the mode of cell movements could be distinct between those regions.

To qualitatively define the nature of local cell movements in the three zones, we performed live imaging using a transgenic mTmG cell membrane reporter at higher resolution and rendered cells in 4D (Fig. 1, F to H, and fig. S3G). Zonal categorization was useful for our analysis because it was based on the predominant type of cell movement in each zone as seen in 2D planes and 3D reconstructions. Cells within the stiff core (zone 1) were least elongated and maintained a stable configuration over time without exchanging neighbors (movies S4 and S5). In zone 2 where a stiffness gradient dominated, cells exhibited collective movement toward the anteroproximal core (movies S6 and S7). Last, in the soft zone (zone 3), cells displayed abundant protrusive activity and underwent frequent neighbor exchanges (movies S8 and S9). These behaviors

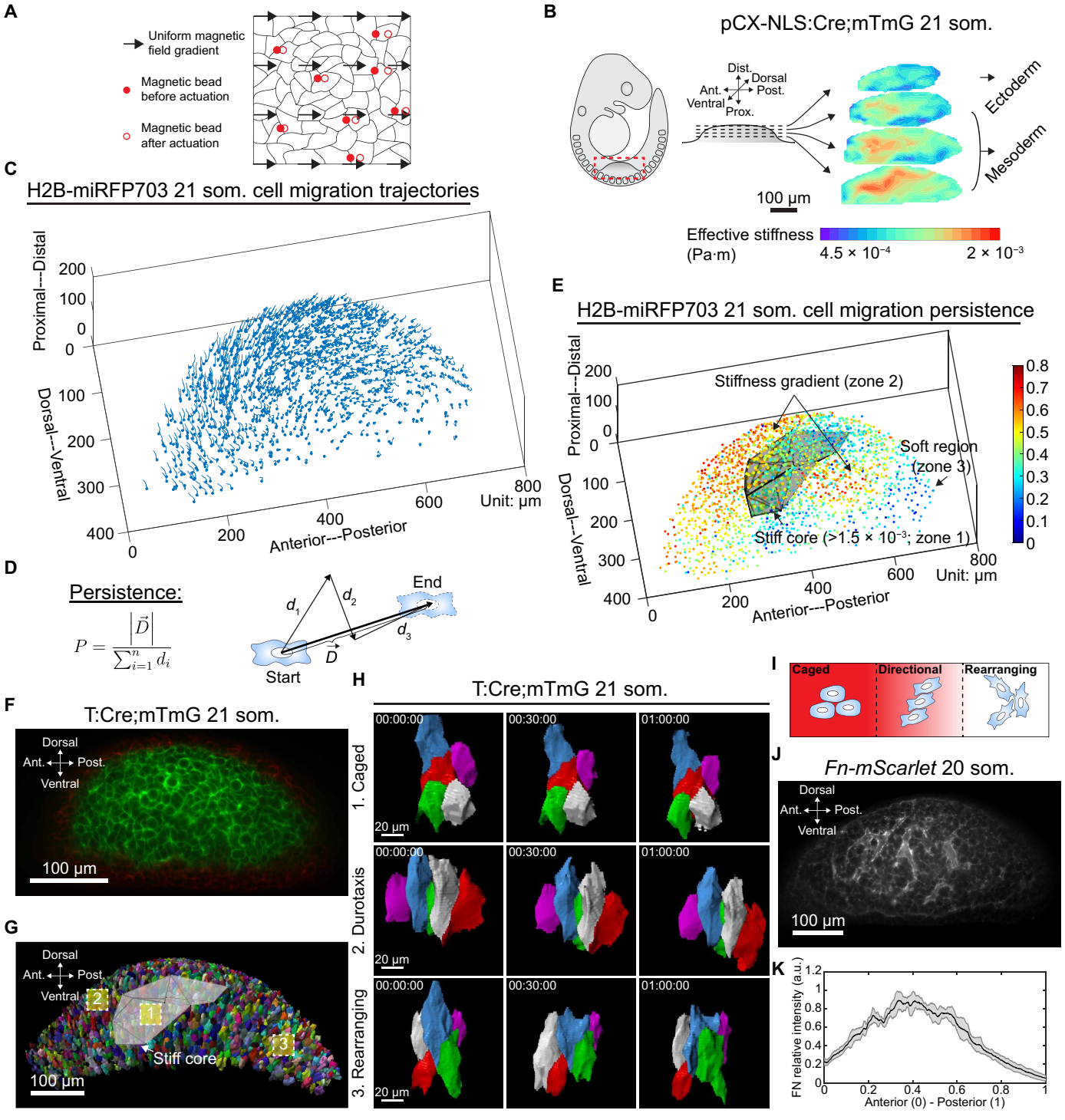

Fig. 1. Regional cell movements correspond to 3D tissue stiffness map. (**A**) Schematic depicting 3D tissue stiffness mapping. (**B**) Slice views of the 20 somite (som.) stage pCX-NLS:Cre;mTmG limb bud stiffness map ($n = 5$). (**C**) H2B-miRFP703 21 som. limb bud 3D mesodermal cell movement trajectories tracked by 3-hour light sheet live imaging. Each dot denotes the last time point of tracking. (**D**) Schematic defining cell migration persistence. (**E**) H2B-miRFP703 21 som. limb bud 3D mesodermal cell migration persistence map overlaid with tissue stiffness map. Gray shade represents the volume mesh of effective stiffness value $>1.5 \times 10^{-3}$. (**F**) A representative *z*-section image of 21 som. T:Cre;mTmG. (**G**) 3D cell membrane rendering of 21 som. T:Cre;mTmG overlaid with tissue stiffness map. Gray shade represents the volume mesh of effective stiffness value $>1.5 \times 10^{-3}$. (**H**) Time-lapse local cell neighbor renderings within the three zones defined in (G) suggesting caged, directional, and rearranging cell movements. (**I**) Proposed zonal cell behaviors as a function of tissue stiffness (red shading). (**J**) A representative *z*-section of 20 som. endogenous FN reporter (*Fn-mScarlet*). (**K**) Relative fibronectin fluorescence intensity profile along anteroposterior axis (average intensity projection of 20 som. *Fn-mScarlet* forelimb *z*-stack, $n = 5$). Gray shading marks the SD. a.u., arbitrary units.

correspond well with relative cell diffusivity measured above. The most basic configuration of cell rearrangement involved a single-cell intercalating into or out of a group of surrounding neighbors that is akin to a 3D topological rearrangement of the first kind (T1) exchange that we encountered previously in the mandibular arch (*2*), although more complex exchanges were also observed. In-between zones, we identified intermediate cell behaviors such as directional movements encountering caged cells (movie S9). On the basis of these observations, we propose that mesodermal cells transition between (1) caged behavior in a stiff environment, (2) directional movement along a stiffness gradient, and (3) rearrangements in a comparatively soft tissue (Fig. 1I).

Fibronectin is required for morphogenetic cell movements

Fibronectin is a key component of ECM that determines embryonic tissue stiffness and has been proposed to underlie durotaxis (*4*, *19*, *23*, *24*). Unlike other ECM components that we previously examined, fibronectin exhibits a spatial gradient that corresponds to mesodermal stiffness in the early limb bud (*4*). To corroborate immunostaining, we generated an endogenous reporter of fibronectin. On the basis of a previous reporter in which overexpressed cells exhibited normal expression and secretion of FN–green fluorescent protein (GFP) in vitro (*25*), a monomeric scarlet fluorophore was inserted in-frame between FN-III domains 3 and 4. A mouse strain was generated using an efficient method of transgenesis known as 2C-HR-CRISPR (Materials and Methods) (*21*). Fn-mScarlet mice were homozygous viable, healthy, and fertile. As expected, the endogenous reporter displayed an anterior-central intensity bias in the early limb bud (Fig. 1, J and K, and movie S11).

By combining nuclear or cell membrane markers with our fibronectin reporter (CMV:Cre;Fn-mScarlet;mTmG), we observed that the large-scale FN mesh moved together with mesodermal cells in the intermediate zone where cells moved directionally (fig. S3, H and I, and movie S12). Within the stiff zone where cells were caged, FN was organized in dense bundles that were stable and seemed to isolate individual cells (fig. S3J and movie S13). In contrast within the soft zone, FN was organized in relatively sparse bundles and pericellular foci that remodeled rapidly and coincidently with dynamic cell rearrangements (fig. S3J and movies S14 and S15). At super-resolution using stimulated emission depletion (STED) microscopy of intact Fn-scarlet embryos, we observed intercellular FN puncta-like nanodomains (*26*). In the stiff region, those domains were abundant and interlinked by linear strands of FN, whereas, in the soft region, they were sparse and relatively isolated (fig. S3J).

Where cells move up a stiffness gradient, it is challenging to distinguish whether haptotaxis [movement of cells up a gradient of cell (integrin)–substrate (fibronectin) binding sites] or durotaxis (movement attributable to the stiffness gradient itself) is dominant because the two phenomena are interrelated. Unlike some migratory populations that use FN as a scaffold upon which they apply tractive forces to move (*27*) such as neural crest cells or myoblasts that move upon a substrate, we see here that limb bud mesodermal cell movements are concurrent with ECM remodeling. This concurrence is a variation of the association between FN remodeling and movements observed between tissue layers in *Xenopus* (*28*, *29*). It suggests that the turnover versus persistence of cell-fibronectin binding sites is a function of fibronectin abundance. We infer that the local stability and remodeling potential of FN are permissive for intercellular movements and tissue phase, a behavior that is not properly captured by the term haptotaxis. At large scale, the graded distribution of fibronectin results in an angular momentum that is akin to the phenomenon of durotaxis. Defining the relative instructive and permissive contributions of cellular motors and ECM remodeling will contribute further insights in this area. Here, we test whether cell movements were causally related to FN density.

To test whether FN underlies tissue stiffness and cell movements in vivo as has been postulated previously (*30*), we genetically manipulated fibronectin expression. *Fn*-null mouse embryos develop normally until E8.0 and exhibit severe malformation of mesoderm-derived structures by E8.5 (*31*). In our study, we conditional deleted homozygous floxed *Fn* (*32*) in mesoderm using T:Cre (T:Cre;$Fn^{f/f}$). T (*Brachyury*) initiates deletion of floxed alleles within mesoderm during late gastrulation, resulting in loss of target proteins by the early limb bud stage (*33*, *34*). Conditional *Fn* mutant embryos were progressively smaller compared to their control littermates between E9.5 and E10.5 (fig. S4, A and B). We confirmed marked depletion of FN in mutant limb buds by immunostaining (fig. S4, C and D). Cell proliferation and apoptosis that were examined by pHH3 immunostaining and LysoTracker staining, respectively, were similar between T:Cre;$Fn^{f/f}$ and wild-type (WT) limb buds in ectoderm and mesoderm at 24 som. (~E9.5) (fig. S4, E and F). At 34 som. (~E10.5), a significant reduction in proliferation and an increase in apoptosis were identified in conditional mutants (fig. S4, G and H).

To examine the effect of fibronectin loss before cell proliferation and apoptosis effects, tissue stiffness mapping was performed at 20 som. in embryos that harbored a cell membrane label (T:Cre;$Fn^{f/f}$;mTmG). Compared to controls, conditional mutants exhibited softer mesoderm that lacked a spatial stiffness bias (Fig. 2A and fig. S5A). By live light sheet imaging of T:Cre;$Fn^{f/f}$;H2B-miRFP703 embryos, the collective pattern of mesodermal cell movements was grossly disrupted with cells in the bulk of the limb bud exhibiting complex, interweaving trajectories (Fig. 2B and movie S16). Correspondingly, cell migration persistence was low throughout the limb bud (Fig. 2C and fig. S5B). Time-lapse evaluation of cell membrane–rendered groups of T:Cre;$Fn^{f/f}$;mTmG cells confirmed widespread intercellular rearrangements that we previously observed only in zone 3 of WT limb buds (Fig. 2, D and E, and movie S17), suggesting that the mesoderm had adopted a comparatively liquid-like character. In loss-of-function mutants, the average track lengths of individual cells were increased, while their coordination was reduced. Distal extension vectors were short and relatively dispersed throughout the bud, and a peripheral domain of converging cells was proportionately broader in compared to WT limb buds (fig. S5, C and D). On the basis of these cell movements, tissue should be misshapen.

Using optical projection tomography (OPT), we found that T:Cre;$Fn^{f/f}$ limb buds developed more symmetrically than those of WT littermates. Mutant limb buds lacked spatial biases such as an anterior peak that normally develops between 20 and 25 som. and a relatively narrow dorsoventral axis. They exhibited a central, short, narrow peak that is consistent with the observed cell trajectories (Fig. 2F and fig. S5, E and F). The short anterior-posterior (AP) axis is reminiscent of previous findings in *Fn*-null embryos (*31*), and the wide dorsal-ventral (DV) axis resembles that of *Wnt5a* mutants (*4*, *35*). Unfortunately, T:Cre;$Fn^{f/f}$ embryos die around E10.75, making it impossible to determine skeletal pattern. Nonetheless, fibronectin is necessary to establish a mesodermal stiffness gradient that regionalizes and orients morphogenetic cell movements that shape the limb bud.

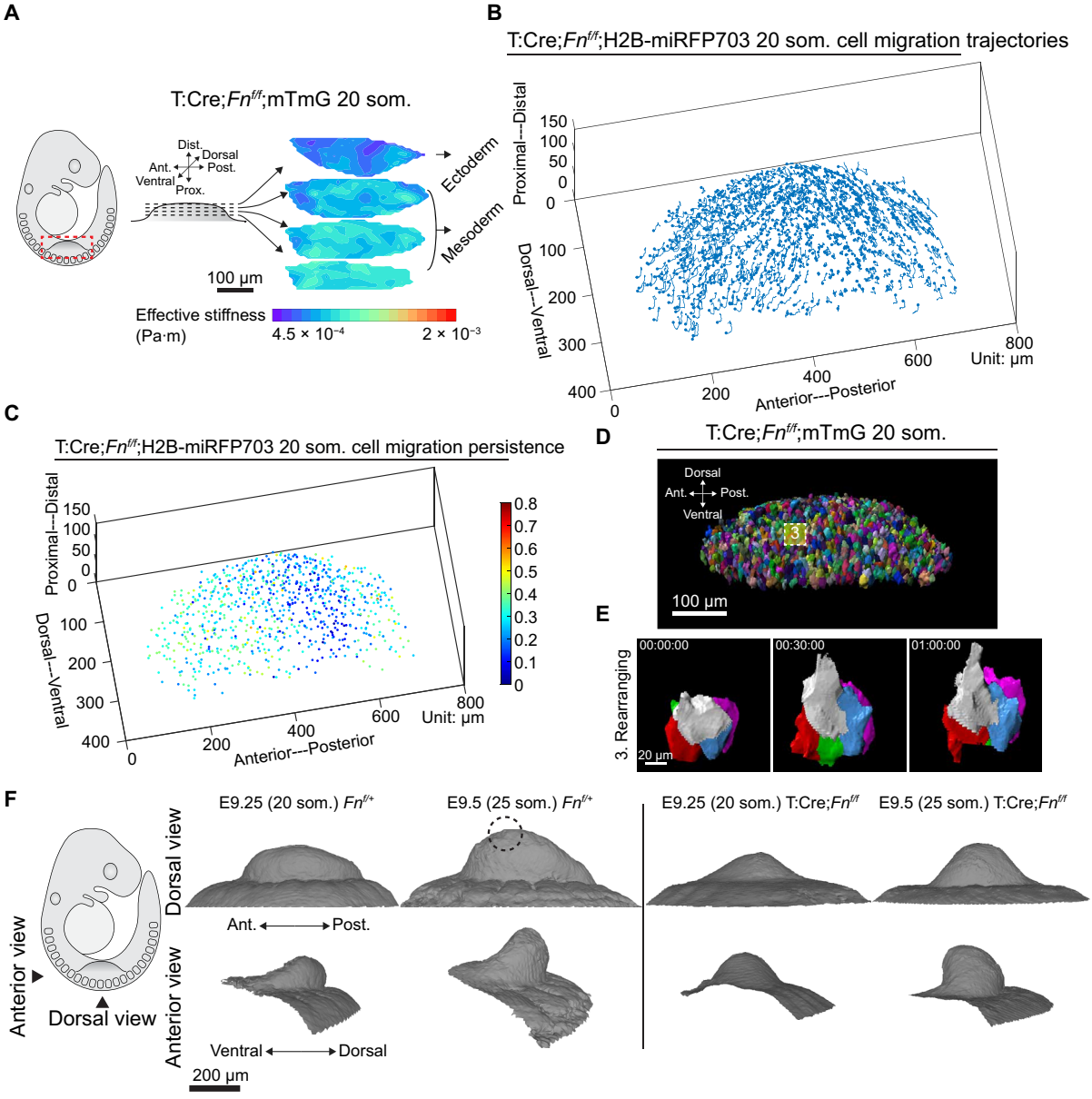

Fig. 2. Loss of fibronectin down-regulates tissue stiffness and leads to a widespread cell rearrangements. (**A**) Slice views of the 20 som. stage T:Cre;*Fn*$^{f/f}$;mTmG limb bud stiffness map ($n = 3$). (**B**) T:Cre;*Fn*$^{f/f}$;H2B-miRFP703 20 som. limb bud 3D mesodermal cell movement trajectories tracked by 3-hour light sheet live imaging. Each dot denotes the last time point of tracking. (**C**) T:Cre;*Fn*$^{f/f}$;H2B-miRFP703 20 som. limb bud 3D mesodermal cell migration persistence map. (**D**) 3D membranes of T:Cre;*Fn*$^{f/f}$;mTmG mesodermal cells rendered from light sheet live imaging. (**E**) Cell neighbor rearrangements occur within in the normally stiff core [dashed square shown in (D)]. (**F**) Limb bud shape change from 20 to 25 som. stage of *Fn*$^{f/+}$ and T:Cre;*Fn*$^{f/f}$ embryos reconstructed from optical projection tomography (OPT). Dashed circle indicates the location of the anteriorly biased peak seen in WT (*Fn*$^{f/+}$) limb buds.

To test the effect of excessive fibronectin, we knocked in a conditional and fluorescently tagged *Fn* transgene to the *Rosa26* locus (R26-CAG-loxP-STOP-loxP-Fn-mScarlet, herein referred to as R26-Fn-mScarlet) using 2C-HR-CRISPR (Materials and Methods) (Fig. 3A and fig. S6A) (*21*). Relative to protein distribution as shown by our endogenous FN reporter (Fig. 1, J and K), overexpression of *Fn* using T:Cre resulted in broader mesodermal distribution of FN as shown by the tagged reporter (Fig. 3, B and C, and movie S18) and by immunostaining (fig. S6, B and C). Tissue stiffness increased widely by magnetic tweezers measurement, abrogating the normal gradient (Fig. 3D and fig. S6D). Live imaging revealed markedly diminished cell movements as indicated by short migration trajectories with low persistence (Fig. 3, E and F, and fig. S6E). Cells maintained stable configurations that lacked neighbor exchanges (Fig. 3, G and H, and movies S19 and S20), suggesting that mesoderm had adopted a predominantly solid-like character. The average angular momentum of the abnormal cell trajectories was reduced, and directional vectors were not coherent (fig. S6, F and G). Therefore, excessive fibronectin is sufficient to stiffen tissue in a manner that cages cell movements.

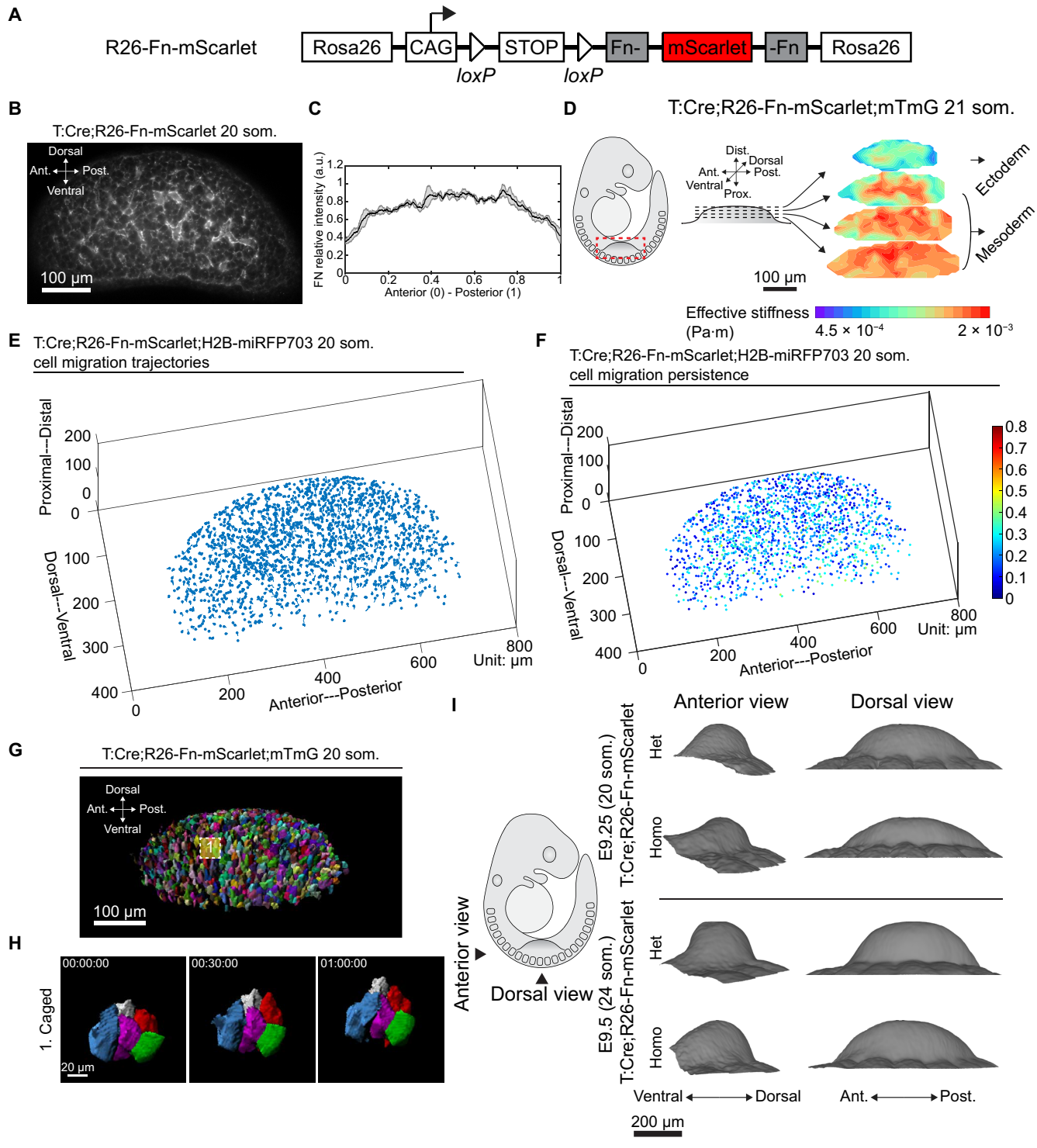

Fig. 3. Fibronectin overexpression up-regulates tissue stiffness and leads to a broadly caged state. (**A**) Conditional Rosa26 fibronectin mScarlet knock-in mouse construct. (**B**) A representative *z*-section image of 20 som. FN-overexpression strain (T:Cre;R26-Fn-mScarlet). (**C**) Relative fibronectin fluorescence intensity profile along anteroposterior axis (average intensity projection of 20 som. T:Cre;R26-Fn-mScarlet forelimb *z*-stack, $n = 3$). Gray shading marks the SD. (**D**) Slice views of the 20 som. stage T:Cre;R26-Fn-mScarlet;mTmG limb bud stiffness map ($n = 3$). (**E**) T:Cre;R26-Fn-mScarlet;H2B-miRFP703 20 som. limb bud 3D mesodermal cell movement trajectories tracked by 3-hour light sheet live imaging. Each dot denotes the last time point of tracking. (**F**) T:Cre;R26-Fn-mScarlet;H2B-miRFP703 20 som. limb bud 3D mesodermal cell migration persistence map. (**G**) Cell membranes of T:Cre;R26-Fn-mScarlet;mTmG limb bud rendered from live light sheet imaging. (**H**) Cells maintain neighbor relationships over time, suggesting a caged state. (**I**) Limb bud shape change from 20 to 25 som. stage of T:Cre;R26-Fn-mScarlet;mTmG embryos.

Like conditional loss-of-function mutants, fibronectin-overexpressing limb buds also lacked spatial biases such as an anterior peak and exhibited a broadened anteroposterior axis (Fig. 3I and fig. S7A), suggesting that the tissue is growing relatively isotropically due to deficient convergent extension. Unlike *Fn* mutants, T:Cre;R26-Fn-mScarlet embryos survived until E14.5, permitting assessment of skeletal pattern by cartilage staining. Transgenic limbs were disproportionately short with marked radial and first digit hypoplasia (fig. S7B). This dysplasia implies that early morphogenetic movements that underlie nuanced limb bud shape also affect pattern formation. Identification of processes downstream of FN that link early limb bud morphogenesis to the skeleton will potentially refine models of pattern formation.

Tissue stiffness predicts the mode of cell movements

The preceding data demonstrate that limb bud mesoderm is a mixed-phase environment. This context is distinct to previously described embryonic tissues such as the zebrafish tail bud and during epiboly in which parameters such as cell packing density (*3*) or cell-cell connectivity (*13*), respectively, define solid and liquid phases at a transitional critical point. In contrast, mammalian mesoderm exhibits a transitional zone of directional cell movement between solid and liquid phases as a function of local ECM-dependent tissue stiffness. We considered whether rigidity phase transition and directional cell movement can be described by a unified mathematical model.

We propose a minimal mathematical description for a stiffness-driven phase transition that includes a description of directional cell movement in the intermediate interpolating region within mixed-phase mesoderm. Starting with a modified Landau theory for second-order phase transitions (*36*), we add a term describing the coupling of cellular diffusion to a stiffness gradient (stiffness phase transition model)

$$E = a(K - K_c)D^2 + bD^4 - c\vec{D} \cdot \vec{\nabla} K$$

where a, b, and c are positive coefficients. In this equation, the first two terms represent the standard Landau phenomenological description for a phase transition with our postulate that there is a fluid to solid transition driven by tissue stiffness, K, above a critical threshold, K_c. As in previous works (*37*), particle self-diffusivity D (Materials and Methods and fig. S7C) is an order parameter for the transition. Diffusivity measures the particle spreading rate in the medium and is an important metric to distinguish the state of matter. It is defined as magnitude of the displacement vector divided by six times the time duration (Materials and Methods). Ordinarily, cells should move down a diffusivity potential as shown in the schematic in Fig. 4A. The last term in our modified Landau equation predicts a tilting of the diffusion potential by the stiffness gradient, resulting in directional cell movement. Our theoretical model suggests that for a zero-stiffness gradient, one would expect the diffusivity to simply transition from a nonzero value at low stiffness (rearranging state) toward zero as stiffness increases (caged state). This postulate is given by a simple sigmoid-type interpolation with the width defining the sharpness of the transition. A real WT limb bud, however, does not exhibit uniform stiffness but rather a region of higher stiffness surrounded by a region of lower stiffness with an intermediate region interpolating between the two. It is more akin to a mixed-phase situation rather than an equilibrium thermodynamic limit. The interpolating region necessarily has a nonzero stiffness gradient and so will have some additional dynamics and a greater magnitude of diffusivity (Fig. 4A).

An empirical cell diffusivity map of the WT limb bud shows a similar pattern compared to cell migration persistence. The stiff and soft zones both exhibit low diffusivity, whereas the stiffness gradient zone has high diffusivity (Fig. 4B) in agreement with our stiffness-phase transition model. By registering the WT cell diffusivity map and tissue stiffness map, we obtained the relation between diffusivity and stiffness allowing us to calibrate the stiffness-phase transition model. The stiffness gradient roughly follows a Gaussian distribution in the WT limb bud (fig. S7, D and E), so we assumed that diffusivity would likewise diverge from the simple interpolation with a Gaussian curve. As such, we fit a sigmoid plus a Gaussian to arrive at our full expected form as shown in Fig. 4C. To test the predictive ability of the model, we calculated cell diffusivity maps of *Fn* conditional loss (T:Cre;$Fn^{f/f}$) and overexpression (T:Cre;R26-Fn-mScarlet embryos) (Fig. 4, D and E) and registered them with tissue stiffness maps. T:Cre;$Fn^{f/f}$ and T:Cre;R26-Fn-mScarlet embryos both abolished the tissue stiffness gradient in limb bud mesoderm, with lower cell diffusivity with T:Cre;R26-Fn-mScarlet (i.e., stiffening) being more significant. The relationship between diffusivity and stiffness in FN-manipulated limb buds follows our model (Fig. 4, F and G), implying that the stiffness modification introduces a predictive component to the Landau phase transition description. Rigidity phase transition and directional cell movement coexist along a continuum in murine mesoderm.

Fibronectin is regulated by feedback involving WNT5A and YAP

Our previous work showed that *Wnt5a* is required for FN expression in the early mouse limb bud (*4*). To identify the relevant pathway, we examined potential downstream signaling components (fig. S8A). A transgenic reporter of the effectors T cell factor/lymphoid enhancer factor (TCF/Lef) and immunostaining against the co-activator β-catenin exhibited no spatial bias in distribution in WT limb buds or a difference in expression levels between WT and $Wnt5a^{-/-}$ limb buds (fig. S8, B to E), suggesting that WNT5A does not activate the canonical WNT pathway. Key signaling components Van Gogh-like 2 (VANGL2) and c-Jun N-terminal kinase (JNK) were also not spatially biased (fig. S8, F to I), suggesting that the noncanonical pathway is also unlikely to transmit WNT5A signal at this early stage of limb development. Unexpectedly, although PCP signaling is important for elongation of skeletal elements during fetal growth (*38*, *39*), the early limb bud appears normal among pathway mutants (*35*, *40*–*43*).

Alternative effectors of WNT5A include YAP/TAZ (*44*), although evidence for that pathway in vivo is lacking. It has also been shown that *Fn* is a downstream target of YAP in vitro (*45*). The expression domain of YAP, but not of phospho-YAP that is retained in the cytoplasm (*46*), colocalized with the FN domain (Fig. 5, A to C, and fig. S9A). We identified a strong correlation between YAP nuclear/cytoplasmic ratio and FN intensity among individual cells (Fig. 5B and fig. S9B). Enrichment of nuclear YAP within the stiff anterior core of the limb bud that we identified by immunostaining was corroborated using an endogenous YAP reporter (fig. S9, C to E, and movie S21) (*47*). Next, we examined whether YAP is necessary for FN by performing conditional knockout of floxed *Yap/Taz* using T:Cre. In *Yap/Taz* mutant limb buds, FN immunostain intensity was broadly diminished (Fig. 5, D and E) and limb bud shapes resembled

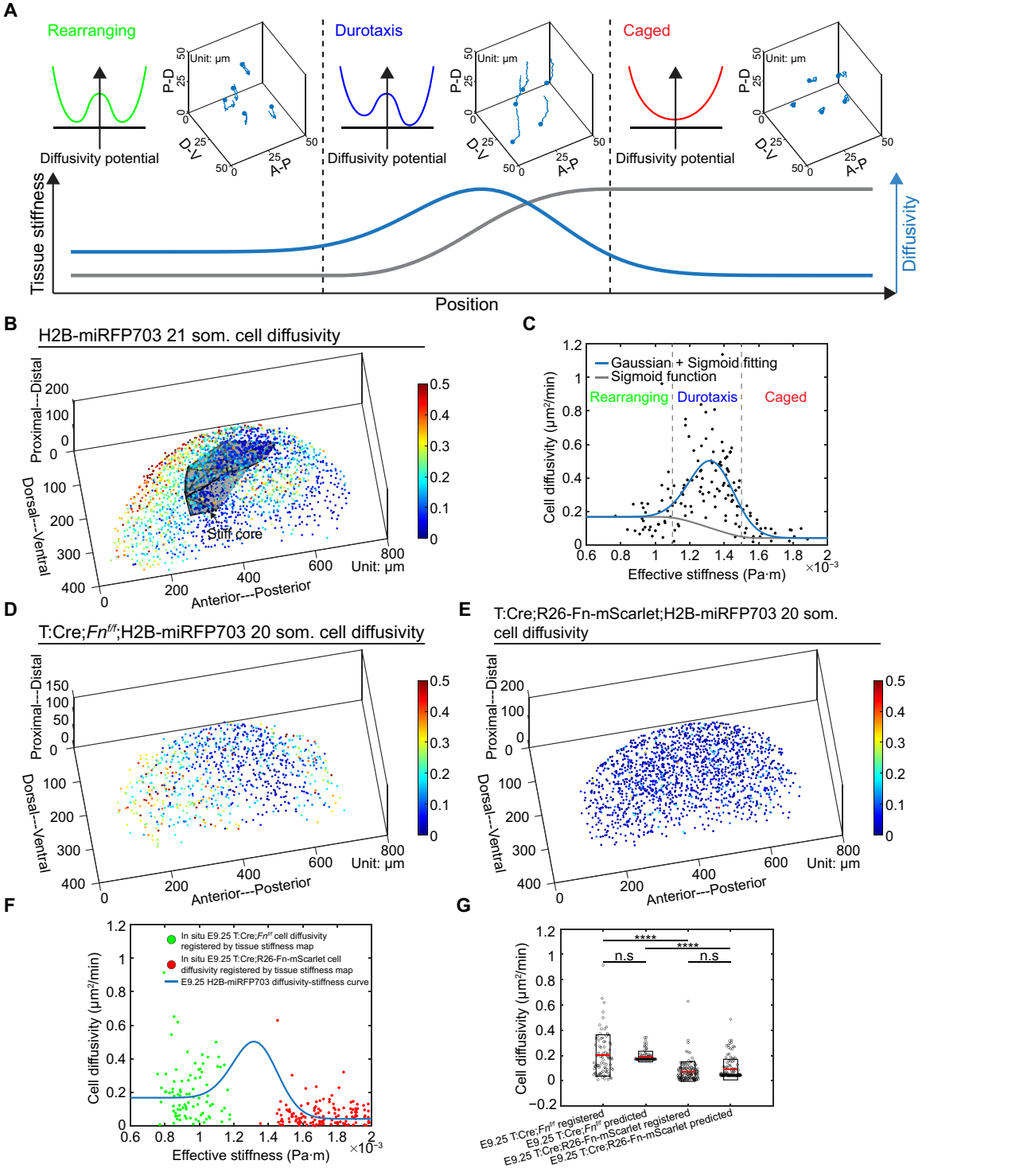

Fig. 4. Prediction of cell behaviors from tissue stiffness map. (**A**) Diffusibility potential as a function of tissue stiffness. P-D, proximal-distal; D-V, dorsal-ventral; A-P, anterior-posterior. (**B**) H2B-miRFP703 21 som. limb bud 3D mesodermal cell diffusivity map overlaid with tissue stiffness map. Gray shading represents the volume mesh of effective stiffness value >1.5 × 10^{-3}. (**C**) Cell diffusivity as a function of tissue stiffness. (**D**) T:Cre;$Fn^{f/f}$;H2B-miRFP703 20 som. limb bud 3D mesodermal cell diffusivity map. (**E**) T:Cre;R26-Fn-mScarlet;H2B-miRFP703 20 som. limb bud 3D mesodermal cell diffusivity map. (**F** and **G**) T:Cre;$Fn^{f/f}$;H2B-miRFP703 and T:Cre;R26-Fn-mScarlet;H2B-miRFP703 limb bud mesodermal cell diffusivities follow the prediction of the stiffness-phase transition model (two-tailed paired Student's *t* test, ****$P < 0.0001$). n.s, not significant.

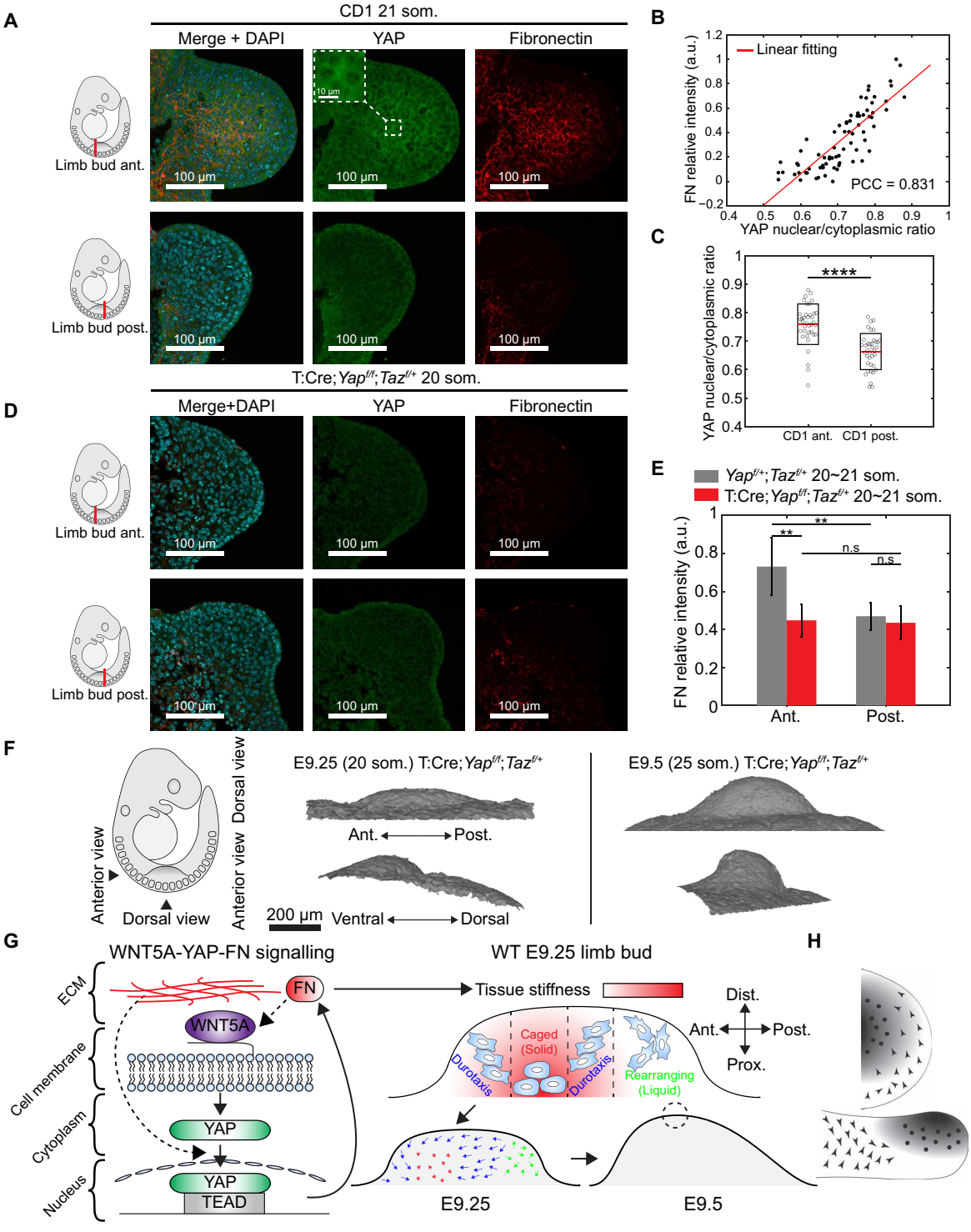

Fig. 5. Feedback mechanism involving Wnt5a-YAP-FN. (**A**) Transverse sections of 21 som. CD1 embryos at forelimb anterior and posterior regions. Sections were stained with 4′,6-diamidino-2-phenylindole (DAPI; cyan) anti-YAP (green) and anti-fibronectin antibody (red). (**B**) Relative fibronectin fluorescence intensity versus YAP nuclear/cytoplasmic ratio of 20 to 21 som. CD1 ($n = 3$) forelimbs. PCC, Pearson correlation coefficient. (**C**) YAP nuclear/cytoplasmic ratio of 20 to 21 som. CD1 embryos ($n = 3$) at forelimb anterior and posterior regions (two-tailed unpaired Student's t test, $^{****}P < 0.0001$). (**D**) Transverse sections of 20 som. T:Cre;$Yap^{f/f}$;$Taz^{f/+}$ embryos at forelimb anterior and posterior regions. Sections were stained with DAPI (cyan) anti-YAP (green) and anti-fibronectin antibody (red). (**E**) Relative fibronectin fluorescence intensity in 20 to 21 som. $Yap^{f/+}$;$Taz^{f/+}$ ($n = 5$) versus T:Cre;$Yap^{f/f}$;$Taz^{f/+}$ ($n = 3$) embryos at forelimb anterior and posterior regions (two-tailed unpaired Student's t test, $^{**}P < 0.01$). Error bars indicate SD. (**F**) Limb bud shape change among T:Cre;$Yap^{f/f}$;$Taz^{f/+}$ embryos from 20 to 25 som. stage reconstructed from OPT. (**G**) Schematic model representing the WNT5A-YAP-FN signaling pathway that establishes tissue stiffness and orchestrates cell movements to drive limb bud shape change. (**H**) Variations in stiffness gradient geometry correspond to patterns of morphogenetic cell movements in the limb bud (top) and mandibular arch (bottom).

those of *Fn* conditional knockouts with greater severity at 20 and 25 som. stages (Fig. 5F). Unfortunately, conditional inactivation of *Yap/Taz* is lethal at around E10.0, making it impossible to determine skeletal pattern. These data suggest YAP is an upstream regulator of FN in vivo.

Various in vitro studies have shown that YAP is translocated to the nucleus on a stiff substrate (*48*–*50*). We found that, in T:Cre;$Fn^{f/f}$ limb buds that exhibit markedly reduced but detectable FN, YAP nuclear/cytoplasmic ratio was diminished and its colocalization with residual fibronectin was disrupted (fig. S10, A to C). *Yap* expression level by quantitative reverse transcription polymerase chain reaction (qRT-PCR) was also down-regulated in *Fn* conditional knockouts (fig. S10D). In fibronectin overexpressing limb buds, the domain of enrichment of nuclear YAP was expanded posteriorly (fig. S10, E to G). The level of *Yap* gene expression remained largely unaffected (fig. S10H), implying protein translocation underlies the nuclear/cytoplasmic ratios that we observed. The mechanical activation of YAP was shown to be triggered by both active and inactive focal adhesion kinase (FAK) (*51*). Our results revealed that the domain of FAK mediating cellular attachment to FN also corresponded to the native and overexpressed FN domains (fig. S10, I to L), suggesting its role in mediating mechanical cues and likely YAP location.

In *Wnt5a* mutants, nuclear localization of YAP was diminished as was *Yap* expression (fig. S11, A to D), implying a potentially dual effect on transcription and protein location. The *Wnt5a* expression domain and level of expression were unaffected in *Yap*-CKO limb buds (fig. S11, E and F). Among T:Cre;$Fn^{f/f}$ limb buds, *Wnt5a* expression level, but not its expression domain by in situ hybridization, was down-regulated (fig. S11, E and G). These data imply that positive feedback by FN is primarily at the level of YAP activation, whereas feedback upon *Wnt5a* is weak. Of course, the direct or indirect effects of these mediators were not tested here.

Because the *Wnt5a* RNA domain is distally biased, it has been difficult to understand how it positively regulates the initial domains of YAP and FN that are biased proximally and anteriorly. In comparison to a negative $Wnt5a^{-/-}$ control, WT WNT5A protein was uniform across limb mesoderm at E9.0 and E9.25 (fig. S11, H to K). In the pre-limb bud lateral plate, a low level of FN is also uniformly present. Later in the 24 som. limb bud, FN expression occupies a broader, more central domain (*4*) that more closely matches the mesodermal WNT5A domain. We infer that the YAP and FN domains lag behind that of WNT5A as the early limb bud expands.

In contrast to the broad limb buds in *Fn* overexpressing embryos that lack skeletal elements, *Wnt5a* mutants exhibit smaller but nearly fully intact skeletal elements (fig. S11L) (*52*). On the basis of their phenotypes, these mediators have overlapping yet distinct functions that likely link early morphogenesis to skeletal pattern by mechanisms that will require different approaches to ascertain. Overall, these data indicate an upstream role for *Wnt5a* in YAP activation and FN expression and feedback by FN primarily upon YAP (Fig. 5G).

DISCUSSION

Our data show that control of morphogenetic cell movements is achieved by tuning fibronectin-dependent tissue stiffness. In bulk mesoderm, stiff regions apparently promote structural stability and relatively isotropic growth, whereas soft regions permit deformability and elongation. In contrast to the inside-out stiffness gradient of the limb bud, the murine mandibular arch exhibits a near reverse gradient (distal/anterior to proximal/posterior) with corresponding reverse orientation of caged and intercalating cell domains (Fig. 5H) (*2*, *24*). The geometry of a stiffness gradient seems to define mesodermal tissue shape. This concept extends earlier observations that effective cell migration occurs at intermediate ECM concentrations, whereas low and high concentrations can inhibit migration by regulating adhesive strength in vitro (*53*) and in vivo (*54*). The directional movement that we observed in the intermediate regime progressively contributes cells and ECM to enlarge the stiff core.

Key findings in this study raise new questions. Our stiffness-phase transition model unifies two concepts that were previously considered separately. Stiffness gradient-dependent, directional cell movements take place in an interpolating region in mixed-phase tissue. It will be interesting to determine whether transitions in cell behavior occur at stiffness thresholds that are absolute or relative. Examination of tissues or embryos that are substantially larger or smaller than the murine limb bud with different tissue properties will be instructive in this regard.

Distinguishing durotaxis from haptotaxis is challenging because the density of cell-ECM binding sites and ECM-dependent stiffness are inherently coupled. Unlike in vitro environments in which substrate stiffness and binding site density can be modified separately by altering polymer or ECM protein concentration within a substrate, stiffness and binding site densities are not readily distinguishable in vivo. Previous inactivation of a fibronectin binding motif (RGD of FN-III) for $\alpha5\beta1/\alpha v$ integrins did not compromise FN matrix assembly (*55*) and resulted in a less severe phenotype than *Fn* null embryos (*31*). However, there were marked mesodermal anomalies including hypoplasia of the limb bud, raising the possibility that cells cannot migrate effectively in the absence of ECM binding sites despite the presence of a matrix that generates a mechanical gradient.

We had initially expected that the large-scale cell movements that we identified would be attributable to codependent durotaxis and haptotaxis. However, our observations that FN remodeling and cell movements are concurrent suggest that the latter concept does not wholly describe mesodermal cell movements in vivo. "Assembly and response" is a long-standing concept that describes how the 3D architecture of ECM affects cell behaviors (*54*, *56*, *57*). Our observation that FN fibrils are associated with directional cell movements but not with cell intercalations is reminiscent of what was shown previously about how the physical state of FN regulates morphogenesis. In *Xenopus*, FN fibrils are required for directional tissue movements such as epiboly but not for cell intercalations during convergent extension that require nonfibrillar FN (*54*, *58*). FN state is therefore permissive for distinct cellular movements and, in turn, likely remodels as a consequence of cellular forces that may alter FN conformation and expose cryptic binding sites for cells and proteins (*54*, *59*). To further define this behavior, it will be useful to interrogate dynamic remodeling of pericellular FN binding sites at molecular resolution and determine the relative contributions of cellular motors and FN density to that process.

Mechanisms that link the early shapes and mechanics of early organ primordia to subsequent pattern formation are far from clear. In this study, altered limb bud shape was associated with later skeletal dysplasia, which resembled that of anterior pattern specification

mutants such as Irx3/5$^{-/-}$ (*60*). We speculate that tissue morphology affects the spatial distribution of morphogens responsible for patterning differentiating cells, for example, by reaction-diffusion (*61*). The geometry of ECM density may also affect the distribution of sequestered ligands that contribute to cell orientation and pattern specification. Defining the distinct and codependent roles of chemical and mechanical contributions to organogenesis remains an important goal.

Previous studies have shown that both WNT signaling and YAP are separately capable of driving fibronectin expression and/or assembly (*62*–*65*). Feedback between cellular behaviors and FN state is facilitated by PCP signaling and FN remodeling in *Xenopus* (*66*), and FN feeds back positively upon Wnt5a in chondrocytes (*67*). Our finding that YAP may be a downstream effector of *Wnt5a* to up-regulate fibronectin raises the possibility that these regulators function in the same pathway also in other contexts. Fibronectin feedback confirms that nuclear translocation of YAP in response to stiff ECM occurs in vivo as had been shown in vitro (*48*, *50*), although ratios of nuclear to cytoplasmic YAP may differ in those contexts.

Our work identifies a layer of morphogenetic regulation by revealing that stiffness-dependent directional cell movement interpolates within mixed-phase tissue. This principle may be more widely applicable but regulated by different ECM components or control variables in other contexts. Identifying key control variables that underlie phase transitions can potentially deepen our understanding of development, the basis of malformations, and advance tissue engineering strategies, in which form is critically important for function.

MATERIALS AND METHODS

Mouse strains

Analysis was performed using the following mouse strains: pCX-NLS:Cre (*68*), mTmG (*69*) [the Jackson Laboratory: Gt(ROSA)26Sor$^{tm4(ACTB-tdTomato-EGFP)Luo}$/J)], R26-CAG-H2B-miRFP703 (*21*) [the Jackson Laboratory: Gt(ROSA)26Sor$^{em1.1(CAG-RFP*)Jrt}$/J], CMV:Cre (*70*) [the Jackson Laboratory: B6.C-Tg(CMV-Cre)1Cgn/J], T:Cre (*71*), FN-mScarlet (see below), *Fn1$^{f/f}$* (*32*) [the Jackson Laboratory: B6;129-Fn1^{tm1Ref}/J], Rosa26-CAG-LSL-Fn-mScarlet (R26-Fn-mScarlet) (see below), *Wnt5a$^{+/-}$* (*52*), TCF/Lef:H2B-GFP (*72*), *Yap$^{f/f}$;Taz$^{f/f}$* (*73*) [the Jackson Laboratory: Wwtr^{1tm1Hmc} Yap1^{tm1Hmc}/WranJ], and YAP-emiRFP670 (*47*). To generate conditional mutant embryos, flox/flox females carrying the appropriate fluorescent reporter were bred to flox/+; Cre males. All strains were outbred to CD1 except for *Fn1$^{f/f}$*, which C57BL/6J background was maintained. All animal experiments were performed in accordance with protocols approved by the Animal Care Committee of the Hospital for Sick Children Research Institute.

Generation of Fn-mScarlet endogenous reporter mouse strain

The endogenous Fn-mScarlet transgene was designed according to a previous publication demonstrating normal expression and secretion of Fn-GFP fusion protein (*25*). The coding sequence of a bright red fluorescence protein mScarlet was placed in-frame between the FN-III domains 3 and 4 coding sequence within the *Fn1* gene. The donor vector with the mScarlet coding sequence spanned by homologous arms: 5′ arm 908 base pairs (bp) and 3′ arm 808 bp, each connected with the mScarlet sequence with a GGGR linker, was synthesized by Epoch Inc. The strain was generated by 2C-HR-CRISPR following our published protocol (*21*). A positive founder was outcrossed for three generations to remove any potential off-target modification from CRISPR genome editing before breeding to establish desired genotypes. Fn-mScarlet mice are homozygous viable, healthy, and fertile. The mouse line was maintained by breeding homozygous mice.

Generation of overexpression Rosa26-CAG-LSL-Fn-mScarlet mouse strain

The Fn-mScarlet overexpression transgene was designed according to a previous publication demonstrating normal expression and secretion of FN-GFP fusion protein (*25*). The coding sequence of a bright red fluorescence protein mScarlet was placed between the FN-III domains 3 and 4 within the full-length cDNA sequence of the longest isoform of mouse Fn1. The full-length Fn-mScarlet cDNA was synthesized by Epoch Inc. and then inserted into the Mlu I restriction site of the pR26 CAG AsisL/Mlu I plasmid (Addgene, 74268; gift from R. Kuehn) (*74*). The strain was generated by 2C-HR-CRISPR following our published protocol (*21*). A positive founder was outcrossed for three generations to remove any potential off-target modification from CRISPR genome editing before breeding to establish desired genotypes. Rosa26-CAG-LSL-Fn-mScarlet mice are homozygous viable, healthy, and fertile. The mouse line was maintained by breeding homozygous mice.

3D tissue stiffness mapping

3D tissue stiffness mapping was conducted using a 3D magnetic device that we developed previously. Briefly, functionalized magnetic beads (Dynabead M280) were microinjected into the limb bud field using a microinjector (CellTram 4r Oil; Eppendor) at anterior, middle, and posterior regions. Multiple depositions were made during one penetration and withdrawal of the needle to distribute the magnetic beads at different depths within the limb bud. The embryo with magnetic beads was placed into the customized imaging chamber and immobilized by Dulbecco's modified Eagle's medium (DMEM) without phenol red containing 12.5% rat serum and 1% low-melt agarose (Invitrogen, lot 16520). The temperature of the imaging chamber was maintained at 37°C with 5% CO_2. Before stiffness mapping, a *z* scan was taken to record the bead locations within the limb bud. Magnetic beads were then actuated by the magnetic device, and bead displacements were recorded by spinning-disk confocal microscopy at the highest frame rate. Bead displacements (in the direction of the magnetic force) were tracked with subpixel resolution and fitted using a Zener model with a serial dashpot in MATLAB to extract the stiffness value. The tissue stiffness mapping dataset was rendered in 3D using a customized python program.

3D limb bud registration

Our 3D limb bud registration was inspired by previous work on segmentation of the full lower limb by computed tomography and construction of an average embryo from multiple reconstructed embryos. The 3D point cloud of the mouse limb bud to be registered (source) was first aligned with the reference (target) in AP and DV axes by translation and rotation. The centroid of the source was then merged with the target. An iterative closest point–based nonrigid registration algorithm was applied until a shape difference below 5% was reached. The shape difference was defined as

$$V_{\text{diff}} = \left| 1 - \frac{V_{\text{source}}}{V_{\text{target}}} \right|$$

where V_{source} and V_{target} are the volumes of source and target, respectively.

Live, time-lapse light sheet microscopy

3D time-lapse microscopy was performed on a Zeiss Lightsheet Z.1 microscope. Embryos were suspended in a solution of DMEM without phenol red containing 12.5% filtered rat serum, 1% low-melt agarose (Invitrogen, lot 16520), and 2% fluorescent beads (1:500; Sigma-Aldrich, lot L5530) that were used for drift compensation within a glass capillary tube. Once the agarose solidified, the capillary was submerged into an imaging chamber containing DMEM without phenol red, and the agarose plug was partially extruded from the glass capillary tube until the portion containing the embryo was completely outside of the tube. The temperature of the imaging chamber was maintained at 37°C with 5% CO_2. Images were acquired using a 20×/0.7 objective with dual-side illumination, and a *z*-interval of 0.5 μm. Images were acquired for 3 to 4 hours with 5-min intervals.

Cell migration tracking and analysis

The light-sheet time-lapse dataset was rendered in Imaris (Bitplane). The positions of cell nuclei and fluorescent beads were tracked over time using an autoregressive motion algorithm. Ectodermal and mesodermal cells were separated on the basis of mean thresholding of fluorescence intensity. Cells undergoing division (based on the morphology of the cell nuclei) were excluded from cell migration tracking. The tracking dataset was then imported into MATLAB (MathWorks), and drift compensation was performed by translation and rotation based on the displacement of fluorescent beads.

Cell migration metrics were calculated using the drift-compensated dataset. Cell migration persistence P was calculated by dividing vector length between the initial and final position by the length of the total trajectory

$$P = \frac{|\vec{d}|}{\sum_{i=1}^{n} d_i}$$

MSD was calculated for individual cells over time. A log-log linear fit was performed to the mean MSD, the slope of which determines the different types of diffusion within limb bud mesoderm. When measuring MSD for any system, the motion will initially appear ballistic until there are enough data beyond the damping time scale of the system, after which the true behavior is apparent (*75*, *76*). To prevent the slope value from being skewed by the initial near ballistic motion, we initiated the fitting from the 2-hour mark. To compute cell diffusivity, as in previous works (*37*), we defined particle self-diffusivity D as

$$D = \frac{|\vec{d}|^2}{6\Delta t}$$

where t is the time in minutes.

To evaluate the cross-embryo difference of the calculated metrics, multiple limb bud datasets were registered to the reference. For each cell in the reference dataset, the closest cell was sought in other datasets within a distance of 20 μm. The SD of each metric was calculated among the cells from different embryos at the site of the reference location.

In the WT drift-compensated cell tracking data, the most obvious motion is the large-scale swirling pattern. To reveal the subtle motions obscured by the swirling pattern, we removed the rotational component by computing the angular momentum of each cell. To find a natural coordinate origin, we identified cells that moved the least (less than 3% of maximum motion) and took their average position. We then computed the angular momentum of each cell around the origin by

$$\vec{l} = \vec{r} \times \overrightarrow{\delta r}$$

where $\vec{r}$ is the vector from our origin to the initial position of the cell and $\overrightarrow{\delta r}$ is the vector from the initial position to the final position. We defined a reference axis by the direction of the average over all the angular momenta and expanded the cell positions in cylindrical coordinates with this new axis as the longitudinal coordinate. Last, we separately plotted the longitudinal (i.e., parallel to the longitudinal cylindrical axis) and radial (i.e., perpendicular to the cylindrical axis) vector components.

Fluorescence lifetime imaging microscopy

Fluorescence lifetime microscopy (FLIM) was performed on a Nikon A1R Si laser scanning confocal microscope equipped with a PicoHarp 300 TCSPC module and a 440-nm pulsed diode laser (Picoquant). Data were acquired with a 40×/1.25 water immersion objective with a pixel dwell time of 12.1 μs/pixel, 512 × 512 resolution, and a repetition rate of 20 MHz. Fluorescence emission of mTFP1 was collected through a 482/35-nm band-pass filter. Embryos were prepared in 50/50 rat serum/DMEM and imaged in a humidified chamber at 37°C in 5% CO_2. Lifetime analysis was performed using FLIMvivo (*77*).

Transmission electron microscopy

Dissected E9.25 mouse embryos were fixed overnight in 2% glutaraldehyde/0.1 M sodium cacodylate buffer. Forelimb bud tissues were dissected and rinsed in 0.1 M sodium cacodylate buffer with 0.2 M sucrose. The tissues were postfixed in 1% osmium tetroxide/0.1 M sodium cacodylate buffer for 1.5 hours and rinsed in 0.1 M sodium cacodylate buffer with 0.2 M sucrose before dehydrated in 70%, 90%, and three times in 100% ethanol. The tissues were infiltrated with propylene oxide, 50% Spurr resin/propylene oxide, and embedded in Spurr resin overnight. Sample blocks were sectioned into 90-nm slices using an ultramicrotome (Leica UC7). Sectioned slices were collected on 200 mesh copper grids and stained with uranyl acetate and lead citrate. Images were acquired using a Hitachi HT7800 TEM, and analysis was performed using ImageJ. Intercellular spaces were measured parallel to and every 100 nm along the cell membrane as the distance between membranes of adjacent cells at forelimb anterior and posterior regions.

STED microscopy

E9.25 Fn-mScarlet embryos were prepared in a #1.5 35-mm glass bottom dish (Ibidi, lot 81218-200) with 50/50 rat serum/DMEM in a humidified chamber at 37°C in 5% CO_2. The heart was removed immediately before imaging, and the embryo was covered with a thin piece of cheesecloth to minimize embryo movement. STED microscopy was performed on a Leica SP8 Lightning confocal microscope with a 93× motCORR STED glycerol immersion objective using 577-nm excitation wavelength and 775-nm depletion wavelength. STED 3D slider, motCORR, and STED 775 delay time were set to 40%, 40%, and 200 ps, respectively. Image deconvolution was performed using Huygens.

Optical projection tomography

Mouse embryos were harvested and fixed in 4% paraformaldehyde overnight at 4°C. OPT was performed using a system that was custom-built and is fully described elsewhere (*78*). 3D datasets were reconstructed from autofluorescence projection images acquired during a 25-min scan period at an isotropic voxel size of 4.5 μm. The limb bud structure was segmented from the embryo and rendered in MeshLab.

Immunofluorescence

Cryosection immunofluorescent staining of embryos was performed as previously described (*4*). Dissected mouse embryos were fixed overnight at 4°C in 4% paraformaldehyde/phosphate-buffered saline (PBS) followed by three washes for 5 min in PBS and incubation in 25% sucrose/PBS overnight at 4°C. Fixed embryos were embedded in O.C.T. Compound (Tissue-Tek, lot 4583) and sectioned into 10-μm slices using a Leica CM1800 cryostat. Sections were washed twice for 5 min in Milli-Q and once for 5 min in PBS, permeabilized in 0.1% Triton X-100/PBS for 20 min, and blocked in 5% normal donkey serum (in 0.05% Triton X-100/PBS) for 1 hour. Sections were then incubated in primary antibody overnight at 4°C followed by four 10-min washes in 0.05% Triton X-100/PBS and then incubated in secondary antibody (1:1,000) for 1 hour at room temperature. Last, sections were washed three times for 5 min in 0.05% Triton X-100/PBS and twice for 5 min in PBS. Images were acquired using a Nikon A1R Si Point Scanning Confocal microscope at ×20 or ×40 magnification, and analysis was performed using ImageJ.

Whole-mount immunofluorescence

Whole-mount immunofluorescent staining of embryos was performed as previously described (*2*). Briefly, mouse embryos were collected and fixed overnight in 4% paraformaldehyde in PBS followed by three washes in PBS. Embryos were permeabilized in 0.1% Triton X-100 in PBS for 20 min and blocked in 5% normal donkey serum (in 0.05% Triton X-100 in PBS) for 1 hour. Embryos were incubated in primary antibody for 5 hours at room temperature followed by overnight incubation at 4°C. They were washed four times for 20 min with 0.05% Triton X-100 in PBS and incubated in secondary antibody for 3 to 5 hours at room temperature. Embryos were then washed four times for 20 min followed by a final wash overnight at 4°C and stored in PBS. Images were acquired using a Nikon A1R Si Point Scanning Confocal microscope at ×20 or ×40 magnification, and analysis was performed using Imaris (Bitplane).

Apoptosis detection

LysoTracker Red DND-99 (Thermo Fisher Scientific, lot L7528) was diluted to 2 μM in DMEM containing 50% rat serum. Embryos were placed in media and incubated in a roller culture apparatus for 1 hour. The temperature was maintained at 37°C with 5% CO_2. Embryos were washed three times with PBS after staining to remove LysoTracker surplus and then fixed overnight in 4% paraformaldehyde in PBS followed by three washes for 5 min in PBS. Images were acquired using a Nikon A1R Si Point Scanning Confocal microscope at ×20 magnification, and analysis was performed using ImageJ.

Whole-mount skeleton staining

Dissected E13.5 mouse embryos in glass scintillation vials were fixed overnight in 70% ethanol at 4°C. The 70% ethanol was removed and replaced with 95% ethanol for 1 hour at room temperature. The embryos were then permeabilized by acetone for 1 hour followed by Alcian blue colorimetric reaction for 1 hour at room temperature. Embryos were kept in 1% KOH overnight at 4°C for clearing. Last, embryos were transferred to 50% glycerol:50% (1%) KOH solution for 2 hours at room temperature and kept in 100% glycerol for long-term storage. For imaging, embryos were transferred to a solution containing 45% sucrose and 40% urea for better imaging quality. Images were captured using a Leica stereo microscope MSV269.

Quantitative reverse transcription polymerase chain reaction

Forelimb bud tissues were dissected at the flank and immediately placed in RNA lysis (RLT) buffer (QIAGEN, lot 79216) for RNA extraction. Total RNA was isolated using an RNeasy Plus Kit (QIAGEN, lot 74136) following the manufacturer's instructions. RNA was quantified on a NanoDrop spectrophotometer (Thermo Fisher Scientific), and equal quantities from control and mutant samples were reverse-transcribed into cDNA using a LunaScript RT SuperMix Kit (New England Biolabs, lot E3010). qRT-PCR was performed using Luna Universal qPCR Master Mix (New England Biolabs, lot M3003) on a ViiA 7 Real-Time PCR System (Applied Biosystems).

Whole-mount in situ hybridization

Whole-mount in situ hybridization was performed after fixation in 4% paraformaldehyde followed by dehydration through a methanol series. Embryos were bleached then underwent digestion in proteinase K; hybridization with probe in formamide, saline-sodium citrate (SSC), SDS, and heparin; treatment with anti-digoxygenin-AP; and colorimetric reaction. WT and mutant littermate embryos were processed identically in the same assay for comparison. Images were captured using a Leica stereo-microscope MSV269.

Antibodies

Primary antibodies included fibronectin (1:100; Abcam, lot ab2413), pHH3 (1:250; Cell Signaling Technology, lot 9706), N-cadherin (1:200; BD Biosciences, lot 610920), β-catenin (1:200; Abcam, lot ab59430), Vangl2 (1:200; Sigma-Aldrich, lot HPA027043), p-SAPK/JNK (1:200; Cell Signaling Technology, lot 9255), YAP (1:200; Abcam, lot ab56701), FAK (1:200; BD Biosciences, lot 610087), phospho-YAP (1:200; Cell Signaling Technology, lot 4911), and WNT5A (1:200; R&D Systems, lot MAB645). Secondary antibodies were purchased from Abcam and used at 1:1000 dilutions: goat anti-mouse immunoglobulin G (IgG) Alexa Fluor (AF) 488 (ab150113), goat anti-rabbit IgG AF 488 (ab150077), and goat anti-rabbit IgG AF 568 (ab175471).

Primers

Primers used in this study included the following: genotyping primers: *Fn-mScarlet* P1, GCAGCCCGGTGTTCAGTACAA; *Fn-mScarlet* P2, CTTGGTCACCTTCAGCTTGGC; *Fn-mScarlet* P3, CCTTTGGTGGCAGATGACCCTTTC; R26 Fn-mScarlet gt, (forward) GTACAACATCACTATCTATGCTGTGGA and (reverse) CGTCCTCGAAGTTCATCACGC; and R26 WT, (forward) CGTGCAAGTTGAGTCCATCCGCC and (reverse) ACTCCGAGGCGGATCACAAGCA; and qRT-PCR primers: Wnt5a, (forward) CTCGGGTGGCGACTTCCTCTCCG and (reverse) CTATAACAACCTGGGCGAAGGAG; Yap, (forward) CCAGACGACTTCCTCAACAGTG and (reverse) GCATCTCCTTCCAGTGTGCCAA; and Ptk2, (forward) ACATCAAGGCGTGTACCTGAGC and (reverse) GTGAGGATGGTCAAACTGACGC.

Supplementary Materials

This PDF file includes:
Figs. S1 to S11
Legends for movies S1 to S21

Other Supplementary Material for this manuscript includes the following:
Movies S1 to S21

REFERENCES AND NOTES

1. B. Boehm, H. Westerberg, G. Lesnicar-Pucko, S. Raja, M. Rautschka, J. Cotterell, J. Swoger, J. Sharpe, The role of spatially controlled cell proliferation in limb bud morphogenesis. *PLOS Biol.* **8**, e1000420 (2010).
2. H. Tao, M. Zhu, K. Lau, O. K. W. Whitley, M. Samani, X. Xiao, X. X. Chen, N. A. Hahn, W. Liu, M. Valencia, M. Wu, X. Wang, K. D. Fenelon, C. C. Pasiliao, D. Hu, J. Wu, S. Spring, J. Ferguson, E. P. Karuna, R. M. Henkelman, A. Dunn, H. Huang, H. Y. H. Ho, R. Atit, S. Goyal, Y. Sun, S. Hopyan, Oscillatory cortical forces promote three dimensional cell intercalations that shape the murine mandibular arch. *Nat. Commun.* **10**, 1703 (2019).
3. A. Mongera, P. Rowghanian, H. J. Gustafson, E. Shelton, D. A. Kealhofer, E. K. Carn, F. Serwane, A. A. Lucio, J. Giammona, O. Campàs, A fluid-to-solid jamming transition underlies vertebrate body axis elongation. *Nature* **561**, 401–405 (2018).
4. M. Zhu, H. Tao, M. Samani, M. Luo, X. Wang, S. Hopyan, Y. Sun, Spatial mapping of tissue properties in vivo reveals a 3D stiffness gradient in the mouse limb bud. *Proc. Natl. Acad. Sci. U.S.A.* **117**, 4781–4791 (2020).
5. M. Cetera, L. Leybova, F. W. Woo, M. Deans, D. Devenport, Planar cell polarity-dependent and independent functions in the emergence of tissue-scale hair follicle patterns. *Dev. Biol.* **428**, 188–203 (2017).
6. I. C. Scott, Life before Nkx2.5: Cardiovascular progenitor cells: Embryonic origins and development. *Curr. Top. Dev. Biol.* **100**, 1–31 (2012).
7. E. H. Barriga, E. Theveneau, In vivo neural crest cell migration is controlled by "Mixotaxis". *Front. Physiol.* **11**, 586432 (2020).
8. K. Minegishi, M. Hashimoto, R. Ajima, K. Takaoka, K. Shinohara, Y. Ikawa, H. Nishimura, A. P. McMahon, K. Willert, Y. Okada, H. Sasaki, D. Shi, T. Fujimori, T. Ohtsuka, Y. Igarashi, T. P. Yamaguchi, A. Shimono, H. Shiratori, H. Hamada, A Wnt5 activity asymmetry and intercellular signaling via PCP proteins polarize node cells for left-right symmetry breaking. *Dev. Cell* **40**, 439–452.e4 (2017).
9. F. Xiong, A. R. Tentner, P. Huang, A. Gelas, K. R. Mosaliganti, L. Souhait, N. Rannou, I. A. Swinburne, N. D. Obholzer, P. D. Cowgill, A. F. Schier, S. G. Megason, Specified neural progenitors sort to form sharp domains after noisy Shh signaling. *Cell* **153**, 550–561 (2013).
10. L. A. Wyngaarden, K. M. Vogeli, B. G. Ciruna, M. Wells, A.-K. Hadjantonakis, S. Hopyan, Oriented cell motility and division underlie early limb bud morphogenesis. *Development* **137**, 2551–2558 (2010).
11. R. Sunyer, V. Conte, J. Escribano, A. Elosegui-Artola, A. Labernadie, L. Valon, D. Navajas, J. M. García-Aznar, J. J. Muñoz, P. Roca-Cusachs, X. Trepat, Collective cell durotaxis emerges from long-range intercellular force transmission. *Science* **353**, 1157–1161 (2016).
12. E. H. Barriga, K. Franze, G. Charras, R. Mayor, Tissue stiffening coordinates morphogenesis by triggering collective cell migration in vivo. *Nature* **554**, 523–527 (2018).
13. N. I. Petridou, B. Corominas-Murtra, C. P. Heisenberg, E. Hannezo, Rigidity percolation uncovers a structural basis for embryonic tissue phase transitions. *Cell* **184**, 1914–1928. e19 (2021).
14. P. F. Lenne, V. Trivedi, Sculpting tissues by phase transitions. *Nat. Commun.* **13**, 664 (2022).
15. M. Merkel, M. L. Manning, A geometrically controlled rigidity transition in a model for confluent 3D tissues. *New J. Phys.* **20**, 022002 (2018).
16. S. Kim, M. Pochitaloff, G. A. Stooke-Vaughan, O. Campàs, Embryonic tissues as active foams. *Nat. Phys.* **17**, 859–866 (2021).
17. C. Parada, S. P. Banavar, P. Khalilian, S. Rigaud, A. Michaut, Y. Liu, D. M. Joshy, O. Campàs, J. Gros, Mechanical feedback defines organizing centers to drive digit emergence. *Dev. Cell* **57**, 854–866.e6 (2022).
18. R. Sunyer, X. Trepat, Durotaxis. *Curr. Biol.* **30**, R383–R387 (2020).
19. A. Shellard, R. Mayor, Collective durotaxis along a self-generated stiffness gradient in vivo. *Nature* **600**, 690–694 (2021).
20. E. A. Audenaert, J. van Houcke, D. F. Almeida, L. Paelinck, M. Peiffer, G. Steenackers, D. Vandermeulen, Cascaded statistical shape model based segmentation of the full lower limb in CT. *Comput. Methods Biomech. Biomed. Engin.* **22**, 644–657 (2019).
21. B. Gu, E. Posfai, J. Rossant, Efficient generation of targeted large insertions by microinjection into two-cell-stage mouse embryos. *Nat. Biotechnol.* **36**, 632–637 (2018).
22. R. Gorelik, A. Gautreau, Quantitative and unbiased analysis of directional persistence in cell migration. *Nat. Protoc.* **9**, 1931–1943 (2014).
23. C. D. Hartman, B. C. Isenberg, S. G. Chua, J. Y. Wong, Vascular smooth muscle cell durotaxis depends on extracellular matrix composition. *Proc. Natl. Acad. Sci. U.S.A.* **113**, 11190–11195 (2016).
24. M. Zhu, K. Zhang, H. Tao, S. Hopyan, Y. Sun, Magnetic micromanipulation for in vivo measurement of stiffness heterogeneity and anisotropy in the mouse mandibular arch. *Research* **2020**, 7914074 (2020).
25. T. Ohashi, D. P. Kiehart, H. P. Erickson, Dynamics and elasticity of the fibronectin matrix in living cell culture visualized by fibronectin-green fluorescent protein. *Proc. Natl. Acad. Sci. U.S.A.* **96**, 2153–2158 (1999).
26. D. Tomer, C. Arriagada, S. Munshi, B. E. Alexander, B. French, P. Vedula, V. Caorsi, A. House, M. Guvendiren, A. Kashina, J. E. Schwarzbauer, S. Astrof, A new mechanism of fibronectin fibril assembly revealed by live imaging and super-resolution microscopy. *J. Cell Sci.* **135**, jcs260120 (2022).
27. J. W. Ramos, D. W. DeSimone, Xenopus embryonic cell adhesion to fibronectin: Position-specific activation of RGD/synergy site-dependent migratory behavior at gastrulation. *J. Cell Biol.* **134**, 227–240 (1996).
28. L. A. Davidson, R. Keller, D. W. DeSimone, Assembly and remodeling of the fibrillar fibronectin extracellular matrix during gastrulation and neurulation in Xenopus laevis. *Dev. Dyn.* **231**, 888–895 (2004).
29. L. A. Davidson, B. D. Dzamba, R. Keller, D. W. Desimone, Live imaging of cell protrusive activity, and extracellular matrix assembly and remodeling during morphogenesis in the frog, Xenopus laevis. *Dev. Dyn.* **237**, 2684–2692 (2008).
30. D. S. Adams, R. Keller, M. A. R. Koehl, The mechanics of notochord elongation, straightening and stiffening in the embryo of Xenopus laevis. *Development* **110**, 115–130 (1990).
31. E. L. George, E. N. Georges-Labouesse, R. S. Patel-King, R. O. Hynes, H. Rayburn, Defects in mesoderm, neural tube and vascular development in mouse embryos lacking fibronectin. *Development* **119**, 1079–1091 (1993).
32. T. Sakai, K. J. Johnson, M. Murozono, K. Sakai, M. A. Magnuson, T. Wieloch, T. Cronberg, A. Isshiki, H. P. Erickson, R. Fässler, Plasma fibronectin supports neuronal survival and reduces brain injury following transient focal cerebral ischemia but is not essential for skin-wound healing and hemostasis. *Nat. Med.* **7**, 324–330 (2001).
33. J. M. Verheyden, M. Lewandowski, C. Deng, B. D. Harfe, X. Sun, Conditional inactivation of *Fgfr1* in mouse defines its role in limb bud establishment, outgrowth and digit patterning. *Development* **132**, 4235–4245 (2005).
34. L. A. Wyngaarden, P. Delgado-Olguin, I.-h. Su, B. G. Bruneau, S. Hopyan, Ezh2 regulates anteroposterior axis specification and proximodistal axis elongation in the developing limb. *Development* **138**, 3759–3767 (2011).
35. K. Lau, H. Tao, H. Liu, J. Wen, K. Sturgeon, N. Sorfazlian, S. Lazic, J. T. A. Burrows, M. D. Wong, D. Li, S. Deimling, B. Ciruna, I. Scott, C. Simmons, R. M. Henkelman, T. Williams, A. K. Hadjantonakis, R. Fernandez-Gonzalez, Y. Sun, S. Hopyan, Anisotropic stress orients remodelling of mammalian limb bud ectoderm. *Nat. Cell Biol.* **17**, 569–579 (2015).
36. L. D. Landau, E. M. Lifshitz, *Statistical Physics* (Elsevier, 2013), vol. 5.
37. D. Bi, X. Yang, M. C. Marchetti, M. L. Manning, Motility-driven glass and jamming transitions in biological tissues. *Phys. Rev. X* **6**, 021011 (2016).
38. B. Wang, T. Sinha, K. Jiao, R. Serra, J. Wang, Disruption of PCP signaling causes limb morphogenesis and skeletal defects and may underlie Robinow syndrome and brachydactyly type B. *Hum. Mol. Genet.* **20**, 271–285 (2011).
39. B. Gao, H. Song, K. Bishop, G. Elliot, L. Garrett, M. A. English, P. Andre, J. Robinson, R. Sood, Y. Minami, A. N. Economides, Y. Yang, Wnt signaling gradients establish planar cell polarity by inducing Vangl2 phosphorylation through Ror2. *Dev. Cell* **20**, 163–176 (2011).
40. Y. Wang, N. Guo, J. Nathans, The role of *Frizzled3* and *Frizzled6* in neural tube closure and in the planar polarity of inner-ear sensory hair cells. *J. Neurosci.* **26**, 2147–2156 (2006).
41. J. Wang, N. S. Hamblet, S. Mark, M. E. Dickinson, B. Brinkman, N. Segil, S. E. Fraser, P. Chen, J. B. Wallingford, A. Wnyshaw-Boris, Dishevelled genes mediate a conserved mammalian PCP pathway to regulate convergent extension during neurulation. *Development* **133**, 1767–1778 (2006).
42. J. P. Mahaffey, J. Grego-Bessa, K. F. Liem, K. V. Anderson, Cofilin and Vangl2 cooperate in the initiation of planar cell polarity in the mouse embryo. *Development* **140**, 1262–1271 (2013).
43. R. Suriben, S. Kivimäe, D. A. C. Fisher, R. T. Moon, B. N. R. Cheyette, Posterior malformations in *Dact1* mutant mice arise through misregulated Vangl2 at the primitive streak. *Nat. Genet.* **41**, 977–985 (2009).
44. H. W. Park, Y. C. Kim, B. Yu, T. Moroishi, J. S. Mo, S. W. Plouffe, Z. Meng, K. C. Lin, F. X. Yu, C. M. Alexander, C. Y. Wang, K. L. Guan, Alternative Wnt signaling activates YAP/TAZ. *Cell* **162**, 780–794 (2015).
45. G. Nardone, J. Oliver-De La Cruz, J. Vrbsky, C. Martini, J. Pribyl, P. Skládal, M. Pešl, G. Caluori, S. Pagliari, F. Martino, Z. Maceckova, M. Hajduch, A. Sanz-Garcia, N. M. Pugno, G. B. Stokin, G. Forte, YAP regulates cell mechanics by controlling focal adhesion assembly. *Nat. Commun.* **8**, 15321 (2017).
46. V. Rausch, C. G. Hansen, The Hippo pathway, YAP/TAZ, and the plasma membrane. *Trends Cell Biol.* **30**, 32–48 (2020).
47. B. Gu, B. Bradshaw, M. Zhu, Y. Sun, S. Hopyan, J. Rossant, Live imaging YAP signalling in mouse embryo development. *Open Biol.* **12**, 210335 (2022).

48. S. Dupont, L. Morsut, M. Aragona, E. Enzo, S. Giulitti, M. Cordenonsi, F. Zanconato, J. le Digabel, M. Forcato, S. Bicciato, N. Elvassore, S. Piccolo, Role of YAP/TAZ in mechanotransduction. *Nature* **474**, 179–183 (2011).
49. V. S. Meli, H. Atcha, P. K. Veerasubramanian, R. R. Nagalla, T. U. Luu, E. Y. Chen, C. F. Guerrero-Juarez, K. Yamaga, W. Pandori, J. Y. Hsieh, T. L. Downing, D. A. Fruman, M. B. Lodoen, M. V. Plikus, W. Wang, W. F. Liu, YAP-mediated mechanotransduction tunes the macrophage inflammatory response. *Sci. Adv.* **6**, eabb8471 (2020).
50. K. E. Scott, S. I. Fraley, P. Rangamani, A spatial model of YAP/TAZ signaling reveals how stiffness, dimensionality, and shape contribute to emergent outcomes. *Proc. Natl. Acad. Sci. U.S.A.* **118**, e2021571118 (2021).
51. D. Lachowski, E. Cortes, B. Robinson, A. Rice, K. Rombouts, A. E. Del Río Hernández, FAK controls the mechanical activation of YAP, a transcriptional regulator required for durotaxis. *FASEB J.* **32**, 1099–1107 (2018).
52. T. P. Yamaguchi, A. Bradley, A. P. McMahon, S. Jones, A Wnt5a pathway underlies outgrowth of multiple structures in the vertebrate embryo. *Development* **126**, 1211–1223 (1999).
53. S. P. Palecek, J. C. Loftust, M. H. Ginsberg, D. A. Lauffenburger, A. F. Horwitz, Integrin-ligand binding properties govern cell migration speed through cell-substratum adhesiveness. *Nature* **385**, 537–540 (1997).
54. T. Rozario, B. Dzamba, G. F. Weber, L. A. Davidson, D. W. DeSimone, The physical state of fibronectin matrix differentially regulates morphogenetic movements in vivo. *Dev. Biol.* **327**, 386–398 (2009).
55. S. Takahashi, M. Leiss, M. Moser, T. Ohashi, T. Kitao, D. Heckmann, A. Pfeifer, H. Kessler, J. Takagi, H. P. Erickson, R. Fässler, The RGD motif in fibronectin is essential for development but dispensable for fibril assembly. *J. Cell Biol.* **178**, 167–178 (2007).
56. C. M. Nelson, M. J. Bissell, Of extracellular matrix, scaffolds, and signaling: Tissue architecture regulates development, homeostasis, and cancer. *Annu. Rev. Cell Dev. Biol.* **22**, 287–309 (2006).
57. R. J. Pelham, Y. L. Wang, Cell locomotion and focal adhesions are regulated by substrate flexibility. *Proc. Natl. Acad. Sci. U.S.A.* **94**, 13661–13665 (1997).
58. L. A. Davidson, M. Marsden, R. Keller, D. W. DeSimone, Integrin α5β1 and fibronectin regulate polarized cell protrusions required for xenopus convergence and extension. *Curr. Biol.* **16**, 833–844 (2006).
59. V. Vogel, M. Sheetz, Local force and geometry sensing regulate cell functions. *Nat. Rev. Mol. Cell Biol.* **7**, 265–275 (2006).
60. D. Li, R. Sakuma, N. A. Vakili, R. Mo, V. Puviindran, S. Deimling, X. Zhang, S. Hopyan, C.-c. Hui, Formation of proximal and anterior limb skeleton requires early function of Irx3 and Irx5 and is negatively regulated by Shh signaling. *Dev. Cell* **29**, 233–240 (2014).
61. R. Sheth, L. Marcon, M. F. Bastida, M. Junco, L. Quintana, R. Dahn, M. Kmita, J. Sharpe, M. A. Ros, Hox Genes regulate digit patterning by controlling the wavelength of a turing-type mechanism. *Science* **338**, 1476–1480 (2012).
62. D. Gradl, M. Kühl, D. Wedlich, The Wnt/Wg signal transducer β-catenin controls fibronectin expression. *Mol. Cell. Biol.* **19**, 5576–5587 (1999).
63. M. Loscertales, A. J. Mikels, J. K. H. Hu, P. K. Donahoe, D. J. Roberts, Chick pulmonary Wnt5a directs airway and vascular tubulogenesis. *Development* **135**, 1365–1376 (2008).
64. B. J. Dzamba, K. R. Jakab, M. Marsden, M. A. Schwartz, D. W. DeSimone, Cadherin adhesion, tissue tension, and noncanonical Wnt signaling regulate fibronectin matrix organization. *Dev. Cell* **16**, 421–432 (2009).
65. D. Kimelman, N. L. Smith, J. K. H. Lai, D. Y. R. Stainier, Regulation of posterior body and epidermal morphogenesis in zebrafish by localized Yap1 and Wwtr1. *eLife* **6**, e31065 (2017).
66. T. Goto, L. Davidson, M. Asashima, R. Keller, Planar cell polarity genes regulate polarized extracellular matrix deposition during frog gastrulation. *Curr. Biol.* **15**, 787–793 (2005).
67. G. Huang, S. Chubinskaya, W. Liao, R. F. Loeser, Wnt5a induces catabolic signaling and matrix metalloproteinase production in human articular chondrocytes. *Osteoarthr. Cartil.* **25**, 1505–1515 (2017).
68. G. Belteki, J. Haigh, N. Kabacs, K. Haigh, K. Sison, F. Costantini, J. Whitsett, S. E. Quaggin, A. Nagy, Conditional and inducible transgene expression in mice through the combinatorial use of Cre-mediated recombination and tetracycline induction. *Nucleic Acids Res.* **33**, 1–10 (2005).
69. M. D. Muzumdar, B. Tasic, K. Miyamichi, N. Li, L. Luo, A global double-fluorescent cre reporter mouse. *Genesis* **45**, 593–605 (2007).
70. F. Schwenk, U. Baron, K. Rajewsky, Acre-transgenic mouse strain for the ubiquitous deletion of loxP-flanked gene segments including deletion in germ cells. *Nucleic Acids Res.* **23**, 5080–5081 (1995).
71. A. O. Perantoni, O. Timofeeva, F. Naillat, C. Richman, S. Pajni-Underwood, C. Wilson, S. Vainio, L. F. Dove, M. Lewandoski, Inactivation of FGF8 in early mesoderm reveals an essential role in kidney development. *Development* **132**, 3859–3871 (2005).
72. A. Ferrer-Vaquer, A. Piliszek, G. Tian, R. J. Aho, D. Dufort, A. K. Hadjantonakis, A sensitive and bright single-cell resolution live imaging reporter of Wnt/ß-catenin signaling in the mouse. *BMC Dev. Biol.* **10**, 121 (2010).
73. A. Reginensi, R. P. Scott, A. Gregorieff, M. Bagherie-Lachidan, C. Chung, D. S. Lim, T. Pawson, J. Wrana, H. McNeill, Yap- and Cdc42-dependent nephrogenesis and morphogenesis during mouse kidney development. *PLOS Genet.* **9**, e1003380 (2013).
74. V. T. Chu, T. Weber, R. Graf, T. Sommermann, K. Petsch, U. Sack, P. Volchkov, K. Rajewsky, R. Kühn, Efficient generation of Rosa26 knock-in mice using CRISPR/Cas9 in C57BL/6 zygotes. *BMC Biotechnol.* **16**, 4 (2016).
75. M. K. Riahi, I. A. Qattan, J. Hassan, D. Homouz, Identifying short- and long-time modes of the mean-square displacement: An improved nonlinear fitting approach. *AIP Adv.* **9**, 55112 (2019).
76. P. H. Wu, A. Giri, S. X. Sun, D. Wirtz, Three-dimensional cell migration does not follow a random walk. *Proc. Natl. Acad. Sci. U.S.A.* **111**, 3949–3954 (2014).
77. K. D. Fenelon, E. Thomas, M. Samani, M. Zhu, H. Tao, Y. Sun, H. McNeill, S. Hopyan, Transgenic force sensors and software to measure force transmission across the mammalian nuclear envelope in vivo. *Biol. Open* **11**, bio065954 (2022).
78. M. D. Wong, J. Dazai, J. R. Walls, N. W. Gale, R. M. Henkelman, Design and implementation of a custom built optical projection tomography system. *PLOS ONE* **8**, e73491 (2013).

Acknowledgments

Funding: This work was funded by the Canadian Institutes of Health Research (168992) to S.H. and Y.S. and the Canada First Research Excellence Fund/Medicine by Design (MbDGQ-2021-04) to S.H. and Y.S. **Author contributions:** Conceptualization: M.Z., B.G., E.C.T., H.T., Y.S., and S.H. Methodology: M.Z., B.G., E.C.T., Y.H., J.R., Y.S., and S.H. Software: M.Z. and E.C.T. Validation: M.Z., H.T., X.C., J.R., and S.H. Formal analysis: M.Z., E.C.T., Y.-K.K., X.C., and Y.S. Investigation: M.Z., B.G., Y.H., Y.-K.K., T.M.Y., X.C., K.Z., E.K.W., and M.R.N. Resources: M.Z., B.G., E.C.T., X.C., X.H., and J.R. Data Curation: M.Z., H.T., and X.H. Visualization: M.Z., E.C.T., X.C., E.K.W., X.H., and Y.S. Supervision: M.Z., R.W., Y.S., and S.H. Writing—original draft: M.Z., B.G., and Y.S. Writing—review and editing: M.Z., B.G., E.C.T., X.C., R.W., J.R., Y.S., and S.H. Project administration: M.Z., Y.S., and S.H. Funding acquisition: R.W., J.R., Y.S., and S.H. **Competing interests:** The authors declare that they have no competing interests. **Data and materials availability:** All data needed to evaluate the conclusions in the paper are present in the paper and/or the Supplementary Materials. Data that support the findings of this study are available at https://figshare.com/articles/dataset/Fibronectin/21779333. All custom codes used in this paper are available at https://zenodo.org/records/10951812 and https://github.com/MinZhuUOTSickKids/Fibronectin. The Fn-mScarlet and R26-Fn-mScarlet mouse strains can be provided by a completed material transfer agreement.

Submitted 29 October 2023
Accepted 14 June 2024
Published 19 July 2024
10.1126/sciadv.adl6366